Non-destructive infrared optoelectronic lock-in carrierography of mc-Si solar cells

Andreas Mandelis*' — Alexander Melnikov* — Jordan Tolev* — Jun Xia* — Syed Huq* — Emmanouil Lioudakis****

** Center for Advanced Diffusion-Wave Technologies, Department of Mechanical and Industrial Engineering, University of Toronto, Ontario M5S 3G8, Canada*
mandelis@mie.utoronto.ca

*** The Cyprus Institute, Energy, Environment and Water Research Center (EEWRC), Guy Ourisson Building, P.O. Box 27456, CY-1645 Nicosia, Cyprus*

ABSTRACT: *A novel non-destructive, non-contact laser-induced infrared lock-in carrierographic imaging technique based on photocarrier radiometry (PCR) was introduced to characterize industrial multi-crystalline silicon solar cells. The modulated photovoltage (MPV) was measured simultaneously with the PCR signal in point-by-point imaging using focused laser scanning. The PCR and MPV signals were also investigated as functions of modulation frequency and load resistance at fixed coordinate points in order to better understand and interpret the physical optoelectronic origins of the carrierographic imaging contrast. A InGaAs-camera based carrierograhic lock-in imaging technique with a spread laser-beam illumination of solar cells was also introduced and was shown to exhibit contrast based on p-n junction RC time constants and on quasi-neutral bulk minority carrier recombination lifetimes.*

KEY WORDS: *photocarrier radiometry, modulated photovoltage, lock-in carrierography, imaging, non-contact.*

Keynote lecture presented at the 10th QIRT Conference

QIRT Journal. Volume 7 – N° 1/2010, pages 35 to 54

1. Introduction

Optical methods, both non-contacting (photoluminescence, PL) and contacting (electroluminescence, EL) are widely used for control of important fabrication parameters of solar cells at all stages of manufacturing so as to optimize efficiency. These methods can successfully control the lateral distribution of lifetime, diffusion length, dark saturation current, series resistance, shunt resistance trapping and dislocations (Kasemann *et al*., 2008, Würfel *et al*., 2007, Fuyaki *et al*., 2005, Isenberg *et al*., 2003, Schubert *et al*., 2006, Breitenstein *et al*., 2008, Kampweth *et al*., 2008, Trupke *et al*., 2006, Glatthaar *et al*., 2009, Macdonald *et al*., 2008). They usually have quasi-static (steady state) character and yield depth-integrated spectroscopic information on radiative emission processes. In a different approach, dynamic spectrally-gated methods with wide range of modulation frequencies can also yield precise information about transport properties of semiconductors. Methods such as solar CELl LOcal characterization (CELLO) FFT impedance analysis, have been utilized for the detailed characterization of local solar cell properties like recombination lifetime, back-side recombination velocity and time constant related to $R_{ser}C_D$, where R_{ser} is the local series resistance and C_D is the local diode capacitance (Carstensen *et al*., 2009). Laser-induced infrared photo-carrier radiometry (PCR) is a dynamic spectrally-gated form of PL and has proven to be an effective non-contacting methodology for the measurement of transport properties in semiconductors (Mandelis *et al*., 2003). PCR is also very suitable for similar applications at the device level, especially junction devices like solar cells for which PCR can potentially yield precise quantitative information about transport and recombination processes. In this paper we report a PCR investigation of industrial polycrystalline (or multi-crystalline, mc) Si solar cells, including a novel dynamic lock-in photocarrier radiometric imaging method ("carrierography") using a fast near-infrared (NIR) InGaAs camera synchronized with a modulated superband-gap laser beam to produce low-frequency optoelectronic images ($\leq$ 10 Hz). We also carried out scanned point-by-point superband-gap laser-beam PCR to generate optoelectronic carrierographic images at high modulation frequencies (> 1 kHz). The term "carrierography" was introduced to indicate the carrier lifetime-dominated nature of our solar-cell imaging contrast. In order to interpret our PCR signals (and ultimately the carrieorographic imaging contrast) in terms of optoelectronic physical processes we performed auxiliary studies comprising PCR and modulated photovoltage (MRV) frequency scans as well as MPV imaging for comparison with our carrierographic images.

2. Materials and experimental set-up

Solar cells featuring a *p-n* junction fabricated on a *p*-type industrial mc-Si wafer (156 x 156 mm^2 area, 200 µm thickness) from Enfoton, Cyprus, were used for measurements. Three mc-Si solar cells and a fragment of a mc-Si solar cell were used in the measurements labelled, and henceforth referred to as, samples 1–3 and "fragment", respectively. PCR frequency-scan measurements from 2 Hz to 100 kHz with focused laser beam were carried out at room temperature with square-wave-modulation. The wavelength of the laser, its spotsize on the solar cell and the output peak power were 830 nm, approx. 400 μm, and 30.9 mW, respectively. Near-infrared radiative emissions from the solar cell were detected using an InGaAs detector (Model PDA400 from Thorlabs) with spectral bandwidth 0.7 - 1.8 μm. The PCR and MPV signals were measured simultaneously using two lock-in amplifiers. A long-pass filter (Model LP-1000 nm from Spectrogon) was used to block the excitation laser beam from the detector. For point-by-point scanning imaging the solar cell was irradiated with the focused laser beam at a fixed modulation frequency leading to high-frequency carrierographic (PCR) images, or at fixed coordinate points leading to single-point PCR frequency scans. MPV imaging was also achieved using the same point-by-point scans and

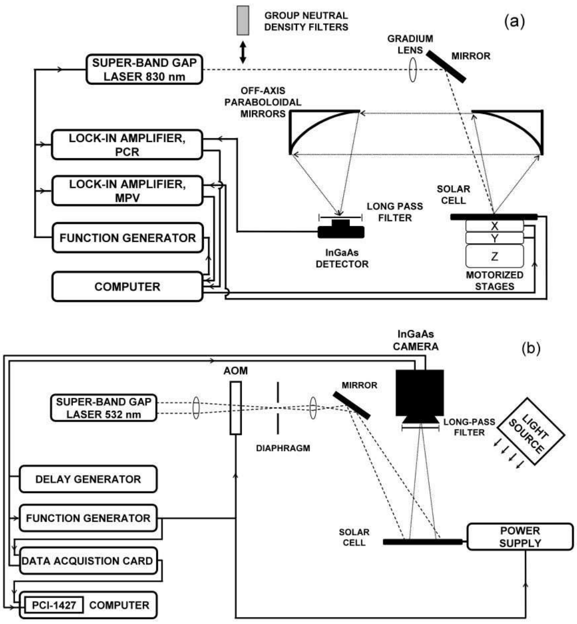

Figure 1. *(a) Experimental set-up for MPV and PCR with focused laser beam and a single-element InGaAs photodiode. (b) Infrared set-up for dynamic lock-in carrierographic solar-cell lock-in imaging.*

recording the photovoltage at each coordinate point. The experimental PCR configuration has been described elsewhere (Mandelis *et al*., 2003) and is shown in Figure 1a.

For lock-in carrierographic camera imaging at low frequencies, a 532-nm solid-state laser (Coherent, model Verdi V-10) in combination with an acousto-optic modulator (AOM) delivered sinusoidally modulated radiation. The laser beam size for area imaging was about 4 cm^2 and maximum frequency was set at 10 Hz. Infrared radiative emissions from the solar cell were detected with a high-speed NIR InGaAs camera (Model SU320KTSW-1.7RT/RS170 from Goodrich Sensors Unlimited) with a 320 x 256 pixel active element and spectral bandwidth 0.9 - 1.7 µm. The camera frame rate was set at 80 Hz so as to attain eight-fold sampling over one period. The camera images were read by the computer using a PCI-1427 frame grabber from National Instruments to produce computer-generated amplitude and phase images. The experimental camera imaging configuration is shown in Figure 1b.

3. Results and discussion

3.1. *PCR and and MPV frequency scans with focused laser beam for various load resistances*

The PCR signal from semiconductors, and Si in particular, depends mainly on radiative emissions from diffusing and recombining minority carrier-wave lifetimes, the ambipolar diffusion coefficient, and front and back surface recombination velocities (Mandelis *et al*., 2003). The centroid of the free-carrier-wave density integral (Mandelis *et al*., 2003)

$$S(\omega) \approx F(\lambda_1, \lambda_2)\int_0^L \Delta N(z,\omega)dz \qquad [1]$$

consists of contributions from radiative recombination mainly in the bulk and at the front surface. In Equation [1], F is a function of the spectral bandwidth $(\lambda_1\ \lambda_2)$ of the IR detector; $\Delta N(z,\omega)$ is the optically generated excess free-carrier-wave density at depth z and angular modulation frequency $\omega = 2\pi f$. Free-carrier-wave density depends on ac carrier diffusion length

$$L_e(\omega) = \sqrt{\frac{D^*\tau}{1 + i\omega\tau}}\ , \qquad [2]$$

as well as on front- and back-surface recombination. For a p-n junction $\Delta N(z,\omega)$ has been calculated elsewhere (Mandelis, 1989, Zhang *et al*., 1991). In Equation [2], D^* is the ambipolar carrier diffusivity and τ is the minority carrier-wave recombination lifetime. By means of Equation [2] the PCR frequency dependence contains information about these transport parameters in the quasi-neutral bulk of the solar cell.

The frequency dependencies of the PCR signal, $S_{PCR}(f)$, and the MPV signal, $V_{ph}(f)$, for sample 1, simultaneously measured with a high–intensity modulated laser beam (peak power about 30.9 mW) in the dark for various load resistances are presented in Figures 2 and 3. The laser excitation point was chosen at mid-distance between electrodes to minimize the effect of series resistance and electrode carrier drain. The amplitude and phase PCR frequency dependencies for $R_L \leq 5.5\ \Omega$ have shapes similar to signals obtained from substrate Si wafers (Mandelis *et al*., 2003).

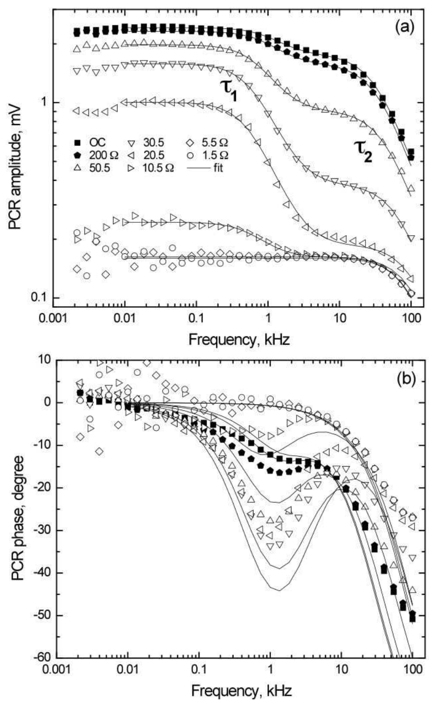

Figure 2. *PCR solar cell frequency dependence with various load resistors (amplitude inset). Laser beam peak power: 30.9 mW; beam spotsize: ~ 400 µm. (a) Amplitude; (b) Phase. Lines represent best fits to Eq. [3] from PCR amplitude data.*

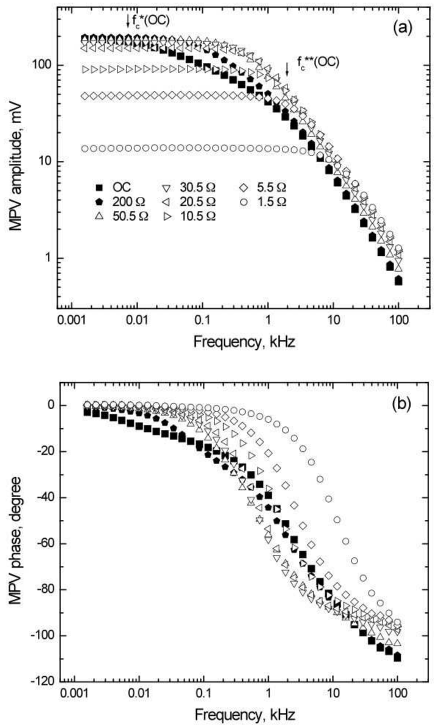

Figure 3. *Frequency dependence of MPV induced with laser beam peak power 30.9 mW; beam spotsize ~ 400 µm. (a) Amplitude, (b) phase. Load resistance, R_L, values are shown in the amplitude figure inset.*

For $R_L \geq 10.5\ \Omega$, the PCR amplitudes exhibit two levels with corresponding phase features. This type of behavior is different from substrate Si wafer PCR signals and is the result of optoelectronic relaxations with two time constants, τ_1 and τ_2. Based on the detailed formulation of the free-carrier-wave model on both sides of the *p-n* junction (Mandelis, 1989, Zhang *et al*., 1991) involving two characteristic lifetimes, the PCR frequency curves were best-fitted to a simplified version of the model (Mandelis, 1989)

$$S_{PCR}(f) = \frac{K_1\tau_1}{1 + i2\pi f\tau_1} + \frac{K_2\tau_2}{1 + i2\pi f\tau_2}, \qquad [3]$$

where K_1 and K_2 are material-property-dependent constants. This expression also shows that the PCR signal amplitudes are proportional to the characteristic carrier-wave lifetimes τ_1 and τ_2.

The best-fitted τ_1 and τ_2 values for various load resistances are presented in Table 1. For all $R_L \geq 10.5\ \Omega$ the longer time constant τ_1 is significantly greater than the shorter time constant τ_2. In order to interpret the origin of time constants PCR and MPV frequency scans have been investigated in more detail.

R_L *(Ω)*	τ_1 *(ms)*	τ_2 *(μs)*
∞ (OC)	0.13	5.2
200.5	0.15	5.0
50.5	0.21	4.0
30.5	0.26	2.6
20.5	0.30	1.7
10.5	0.24	2.0
5.5	-	2.0
1.5	-	1.9

Table 1. *Extracted solar cell time constants for Sample 1 from S_{PCR} amplitude data best-fitted to theory, Eq. [3], for various load resistance values.*

To describe the MPV characteristics of the solar cell, a suitable equivalent circuit model was used as shown in the inset of Fig. 4b, similar to Munakata *et al*. (1981) which used a comparable MPV set-up. Series resistance was neglected for simplicity. For small signal excitation the ac photovoltage V_{ph} can be expressed as

$$V_{ph}(f) = I_{ph}\left(\frac{1}{R_j} + \frac{1}{R_L} + i2\pi f C_j\right)^{-1} \qquad [4]$$

where I_{ph} is the photocurrent, $R_j = dV/dI$ is the dynamic junction resistance, R_L is the load resistance, and C_j is the junction capacitance, the sum of depletion layer capacitance and diffusion capacitance. The cut-off frequency, f_c, is defined as

$$f_c = \frac{(1/R_j) + (1/R_L)}{2\pi C_j}. \qquad [5]$$

The *RC* time constant, τ_{RC} is given by

$$\tau_{RC} = \frac{1}{2\pi f_c}. \qquad [6]$$

The cut-off frequency, f_c, or time constant, τ_{RC} , also depends on the *p-n* junction voltage by virtue of its dependence on $R_j(V)$ and $C_j(V)$.

As shown in Figure 3 the open-circuit (OC) MPV amplitude curve and those at high-load resistances (R_L>30.5 Ω) exhibit two pronounced bending points ("knees") f_c^* and f_c^{**} with corresponding slope change features in the phase-frequency responses. The first knee f_c^* shifts to higher frequency with decreasing load resistance until it merges with the second knee, f_c^{**}, for $R_L \approx 20.5$ Ω. These features can be explained through a change in τ_{RC} with photovoltage across the junction under the high-laser-intensity (2.46 W cm^{-2}) square-wave pulse. When the excitation pulse starts, τ_{RC} and the cut-off frequency correspond to values of R_j, C_j, and R_L for $V_{ph} \approx 0$ while by the end of the square pulse they correspond to R_j, C_j, and R_L for $V_{ph} >> 0$. The difference between the two values results in the appearance of two bending points in the $V_{ph}(f)$ dependence of photovoltage for high excitation intensity.

This interpretation is further supported by more physical insights on the origins of the V_{ph} frequency response obtained using a digital oscilloscope (Tektronix DPO7104) to observe the non-demodulated photovoltage. Figure 4a reveals that the first knee f_c^* is the result of the increase in baseline photovoltage, V_b, with increasing frequency. On the other hand, the second knee f_c^{**} is due to the decrease of the peak photovoltage, V_p, with increasing frequency at higher frequencies. The frequency dependences of V_b and V_p saturate and nearly merge to a single value, V_s , at *ca.* 100 kHz. The value of V_p under the laser excitation pulse is determined by I_{ph} at the laser peak power, f, and R_L, as well as R_j and C_j at the peak photovoltage. The value of V_b is the result of voltage decay after the end of the excitation pulse and it is determined by R_L, R_j and C_j at the baseline photovoltage. The calculated dependence of f_c, Equation [5], on photovoltage across the junction from 0 V to V_p is also shown for several load resistances in Figure 4a. $C_j(V_{ph})$ was determined from the MPV frequency scan at small signal $(V < kT/q)$ and the value of $R_j(V)$ from the *I-V* characteristics of the solar cell (Melnikov *et al*., 2010). The dependence $f_c(V_{ph})$ shifts

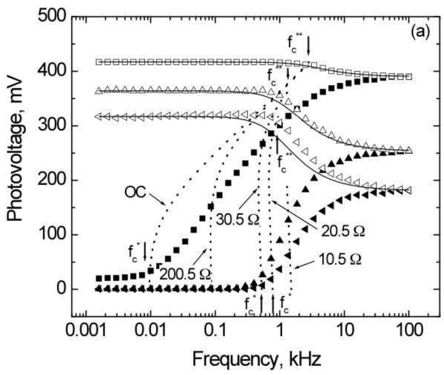

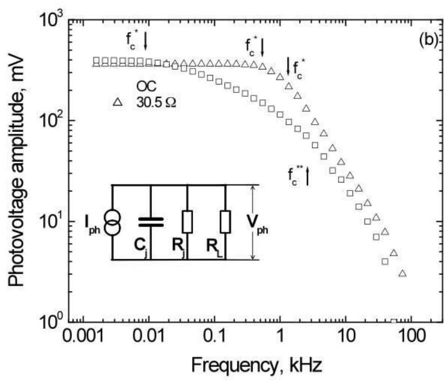

Figure 4. *(a) Frequency dependence of peak (V_p) and baseline (V_b) values of V_{ph} induced with the same square waveform as Fig. 3, laser peak power 30.9 mW_L and beam spotsize ~ 400 µm for various values of load resistance, measured with an oscilloscope; ■ – baseline for OC, □ – peak for OC, ▲ - baseline for 30.5 Ω, △ - peak for 30.5 Ω, ◀ - baseline for 20.5 Ω, ◁ - peak for 20.5 Ω, – theory, Eq. 4. The dotted lines represent calculated f_c dependence on photovoltage with several load resistances; (b) Frequency dependence of the amplitude value V_p - V_b for OC and load resistance 30.5 Ω.*

to higher frequencies with decreasing load resistance and the value of f_c strongly increases with increasing photovoltage at OC. The rate of change in f_c with photovoltage decreases with decreasing load resistance as shown in Figure 4b and f_c remains practically fixed for $R_L \leq 20.5\ \Omega$. The first bending point f_c^* in the frequency dependence of V_{ph} corresponds to the value of f_c at $V_b \approx 0$ V across the junction. The second bending point f_c^{**} corresponds to the cut-off frequency for V_p at modulation frequency $f << f_c^{**}$. The difference between cut-off frequencies for baseline voltage and for peak voltage strongly decreases with decreasing load resistance and practically disappears for $R_L < 20.5\ \Omega$ as shown by the dotted lines in Figure 4a. As a result, the behavior of the MPV is determined mainly by the τ_{RC}^* corresponding to baseline photovoltage and the τ_{RC}^{**} corresponding to peak voltage. In summary, for high-intensity laser-beam excitation the frequency dependence of the MPV is characterized by two knees that merge under small-load resistance conditions. The high-frequency knee is due to τ_{RC} corresponding to the peak signal photovoltage. The low-frequency bending point is determined by the τ_{RC} corresponding to photovoltage near 0 V.

Comparison of the $S_{PCR}(f)$ and $V_{ph}(f)$ frequency dependencies shows that the longer PCR lifetime (τ_1) corresponds to the second knee of the $V_{ph}(f)$ frequency dependence, f_c^{**}, and its origin must be sought at the junction τ_{RC}^{**}. The shorter PCR lifetime (τ_2) is the result of minority carrier recombination in the quasi-neutral bulk *p*-type region. Due to the large junction capacitance of large-size solar cells, a significant number of free minority photocarriers is involved in near-junction charge transfer processes leading to reduction of excess minority carrier density available for recombination at frequencies $f > f_c^{**}$ in the laser-beam-excited area. An absence of features in the $S_{PCR}(f)$ curve at f_c^* can be explained by the small concentration of excess minority carriers at *p-n* junction voltages near 0 V. It is important to note the absence of a $S_{PCR}(f)$ knee with longer time constant τ_1 for $R_L \leq 5.5\ \Omega$. Probably this effect is caused by the delocalization of excess minority carriers generated inside the laser-excited area as the result of the low series resistance and the subsequent elimination of charge discharge processes at the illuminated junction.

3.2. *Localized PCR and MPV frequency scans with focused laser beam*

PCR and simultaneous MPV frequency scans under open circuit conditions at locations across a mc-Si solar cell (Sample 2) are presented in Figures 5 and 6, respectively. Coordinate points were chosen at mid-distance between grid electrodes and marked in the inset of Figures 5b and 6a.

The PCR amplitudes vary significantly over the set of the selected points, nevertheless, all frequency dependencies exhibit two pronounced levels/slopes with corresponding features in the respective phase-frequency responses. Table 2 shows the calculated values of τ_1 and τ_2 from the PCR frequency responses. The measured values of τ_1 corresponding to the junction RC time constants, are very similar, which confirms the uniformity of the device junction geometry. However, the measured τ_2 corresponding to carrier recombination lifetimes in the bulk quasi-neutral region at the various locations are quite different. This fact confirms the inhomogeneous distribution of lifetimes across the mc-Si solar cells. It was also observed that higher PCR amplitude corresponds to longer carrier recombination lifetime, τ_2, as expected from the structure of Equation [3].

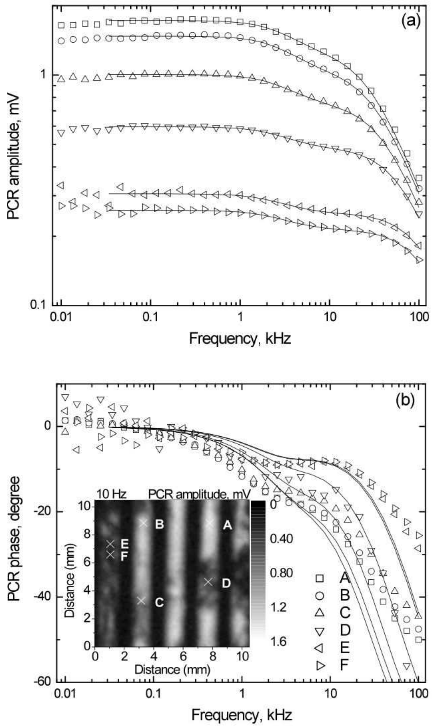

Figure 5. *PCR frequency dependence of a mc-Si solar cell (Sample 2) at various coordinate locations. Laser beam peak power: 30.9 mW and beam spotsize: ~ 400 µm. (a) Amplitude; (b) phase.*

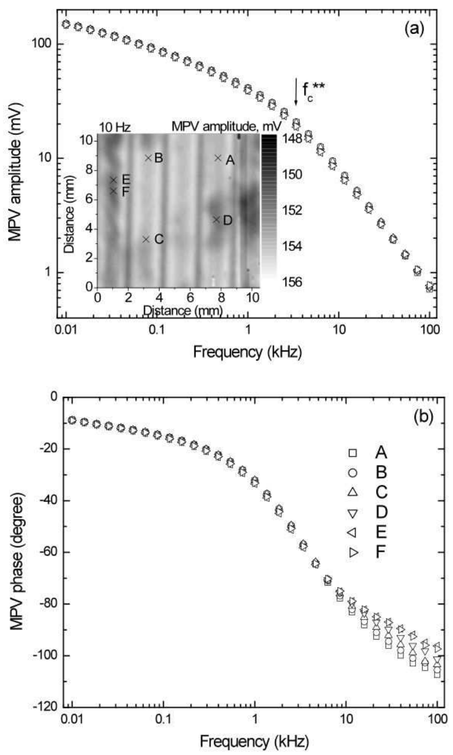

Figure 6. *MPV frequency dependence of the solar cell of Figure 5 at the same coordinate locations. Laser beam peak power: 30.9 mW and beam spotsize: ~ 400 µm. (a) Amplitude, (b) phase.*

Unlike the PCR frequency dependence, the MPV frequency response is significantly less sensitive to the spatial distribution of the transport parameters and non-radiative recombination centers in the solar cell. Figure 6 shows that all MPV curves are practically superposed. The MPV dependences exhibit a clearly pronounced knee, f_c^{**}, corresponding to the RC time constant at large photovoltages generated by the focused high-intensity laser beam (arrow). It is interesting to note that the MPV phases exhibit point-to-point variation at frequencies in the 10 - 100 kHz range. This may be the result of inhomogeneous surface recombination effects due to the short photocarrier-wave diffusion length at those frequencies.

In summary, the PCR frequency response is much more sensitive to optoelectronic inhomogeneities at the junction and in the quasi-neutral regions of mc-Si solar cells than the MPV frequency response which also requires electrical contacts and therefore is of a less localized nature than the PCR response.

Position	Amplitude at 116 Hz (mV)	τ_1 (ms)	τ_2 (μs)
A	1.7	0.048	5.6
B	1.5	0.048	5.1
C	1.0	0.050	4.1
D	0.60	0.053	2.7
E	0.31	0.057	1.6
F	0.26	0.056	1.5

Table 2. *Extracted solar cell time constants from S_{PCR} amplitude data best-fitted to theory, Eq. (3), for various locations on Sample 2.*

3.3. *Point-by-point scanned carrierographic (PCR) and MPV solar-cell images*

Point-by-point scanned carrierographic (PCR) and MPV images of solar-cell Sample 1, obtained with a focused laser beam (spotsize 24 μm, peak power 30.9 mW) at 10 Hz and 100 kHz and obtained simultaneously are shown in Figs.7 and 8 respectively. The PCR images demonstrate a high degree of inhomogeneity across the solar cell caused by various kinds of defects and grain boundaries with high concentration of non-radiative centers.

At 10 Hz contrast is exhibited only by the PCR amplitude image and resolution is similar to the dc or quasi-steady PL image. The PCR phase image exhibits no contrast at low frequencies ≤ 1 kHz (see Fig. 7b) as the long carrier-wave diffusion length is dominated by bulk recombination. High-frequency PCR images show high contrast and much improved feature spatial resolution in both amplitude and phase. The dependence of imaging contrast on the carrier-wave ac diffusion length, Eq. (2) is a manifestation of the depth-profilometric nature of carrierographic imaging. The MPV images show the same features as the PCR images, because the photocurrent depends on the same recombination processes. However, the low-frequency MPV amplitude and phase image contrast and lateral spatial resolution are much poorer. It is important to note that, unlike PCR phases, MPV phase contrast exists even at the lowest frequency (10 Hz). This is a consequence of the involvement in photovoltage generation of free minority photocarriers from the very-near-surface region captured by the adjacent electrodes and channeled to the external circuit, an indication that MPV does not have significant depth-profilometric properties, but is mostly a surface optoelectronic effect.

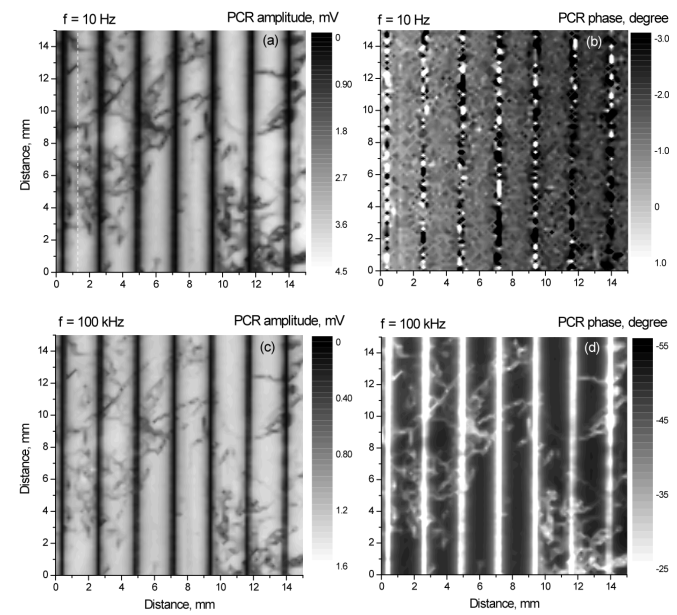

Figure 7. *Lock-in carrierographic (PCR) amplitude (a, c) and phase (b, d) images of a mc-Si solar cell (Sample 1) at 10 Hz (a, b) and 100 kHz (c, d). Images were constructed from point-by-point focused laser-beam scans with 100-µm step with 24-µm spotsize. Laser wavelength and peak power were 830 nm and 30.9 mW, respectively.*

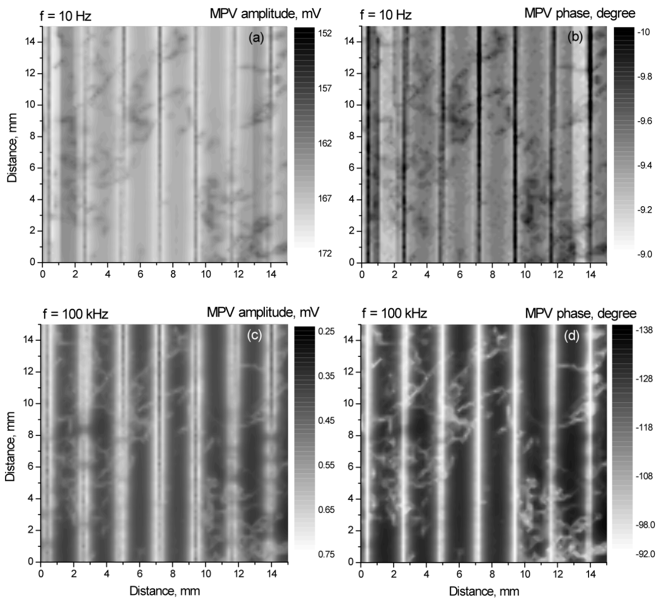

Figure 8. *Lock-in MPV amplitude (a, c) and phase (b, d) images of the solar cell of Figure 7 at 10 Hz (a, b) and 100 kHz (c, d). Images were constructed using the same laser and scanning parameters as in Figure 7.*

Point-by-point PCR and MPV line scans along a vertical line midway between adjacent electrodes in Figure 7a were obtained at 10 Hz and 100 kHz and are shown in Figure 9. These line scans clearly show excellent correlation between PCR and MPV along the solar cell inter-electrode strip in agreement with the images in Figures 7 and 8, including the much lower contrast dynamic range and spatial resolution of the MPV amplitude. The PCR and MPV amplitude dips and phase-lag peaks are the result of beam crossing non-radiative recombination-promoting grain boundaries which decrease the carrier-wave density (amplitude) and shift the phase lag to smaller values, closer to the front surface, due to enhanced recombination or trapping. The low-frequency PCR phase scans are less sensitive to those defects and grain boundaries, as deeper subsurface contributions to the carrier-wave spatial integral in Equation [1] tend to mask the effects of the near-surface recombination centers.

The optimum amplitude contrast occurs at frequencies at which the ac diffusion length is commensurate with the subsurface depth of a recombination center. At grain boundaries acting as non-radiative recombination centers, this appears to occur at ca. 10 Hz for PCR. The MPV amplitude signal shows measurable contrast at low frequencies, whereas the MPV phase contrast is best, and very similar to the PCR phase, at the highest frequencies (here: 100 kHz). The reason for these MPV amplitude differences is the series resistance of the solar cell which further dampens the free photo-excited carrier density wave away from its generation location, while diffusing toward the closest electrode for collection and conversion to photovoltage: The exponential spatial decay of the diffusing carrier wave with its characteristic ac diffusion length (Mandelis, 2001) effectively blocks carrier collection from generation distances longer than $L_e(\omega)$.

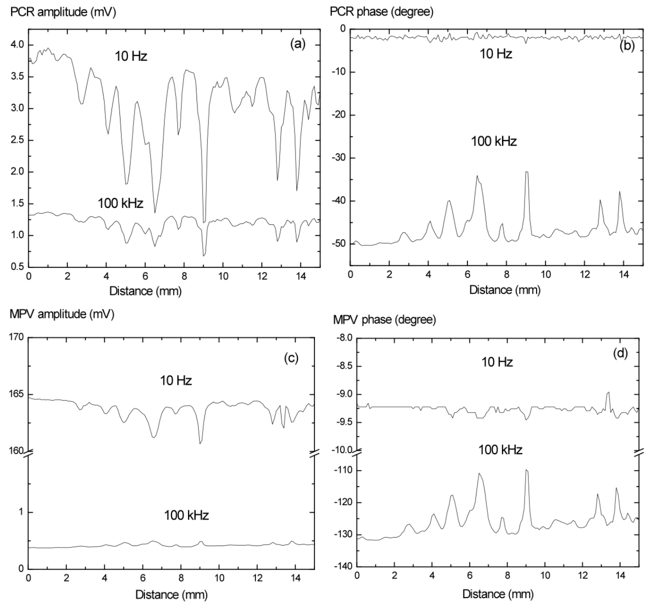

Figure 9. *Vertical PCR and MPV line scans with 100-µm step along the dashed line in Figs. 7a at 10 Hz and 100 kHz. a) PCR amplitude; b) PCR phase; (c) MPV amplitude; (d) MPV phase. Laser beam peak power: 30.9 mW, beam spotsize: 24 µm.*

3.4 *Lock-in carrierography of intact and surface-damaged mc-Si solar cells*

A small area on the surface of an mc-Si solar cell (Sample 3), was mechanically damaged through rubbing with sandpaper. The mechanical treatment led to the destruction of the *p-n* junction and the consecutive reduction of the shunt resistance value from 2870 Ω to 276 Ω and finally to 157 Ω. Resistance was determined from the linear part of the current-voltage characteristics. The InGaAs camera, Fig. 1b, captured images at 10 Hz, the maximum possible rate for our current state-of-the-art carrierographic lock-in imaging, before and after damage. The resulting images following conversion to lock-in amplitudes (phases do not exhibit measurable contrast at 10 Hz) are shown in Figure 10.

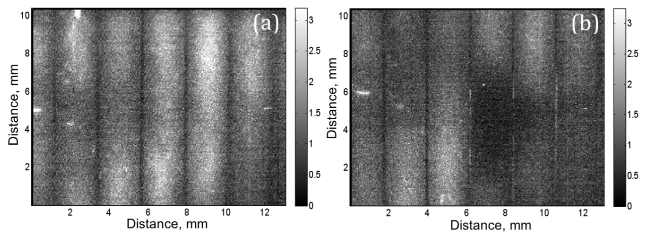

Figure 10. *Lock-in carrierographic camera amplitude images before (a) and after (b) induced mechanical damage on the front side of the solar cell Sample 3 to create an ohmic shunt.*

The damaged areas appear dark as expected from the low photocarrier density and short recombination lifetime, Equation [3], at those locations. PCR and MPV frequency scans at two points outside and inside the damaged area with large changes in shunt resistance, respectively, are presented in Figure 11. The PCR and MPV responses from the point outside the damaged area are similar to those with load resistance as a variable, as discussed earlier on. However, the PCR amplitude and phase frequency curve shapes at the point inside the damaged area changed drastically after the mechanical damage: with a large reduction in amplitude, they became similar to those typical of Si substrate wafers, with only one bending point (Mandelis *et al.*, 2003).

These effects are caused by a significant increase of the surface recombination velocity and the compromised ability of the *p-n* junction to perform its charge separation tasks, thereby rendering the optoelectronic behavior of the solar cell device essentially into that of partly damaged bulk silicon with a poor junction and short recombination lifetime. The MPV amplitude from the damaged area also shows changes (decrease) but the frequency curve shapes remain similar to those before the damage, an indication that the junction separation and electrode collection abilities were not entirely annihilated, in agreement with the PCR results. These results are consistent with the free-carrier-density radiative-emission character of our lock-in carrierographic imaging contrast mechanism.

It is important to note that the contrast of carrierographic PCR amplitude images constructed from point-by-point focussed laser-beam scans, Figure 7a, is higher than that of camera-generated images, such as Figure 10. The former superior contrast is due to the considerably higher intensity of the focussed laser beam and, therefore, the much higher excess photocarrier-wave density than that generated with the broad laser beam illuminating the solar cell imaged with the InGaAs camera. The effective free photocarrier-wave density increases using a small-area (approx. 10 cm^2) solar-cell fragment, because a decreased active area decreases the cell-wide junction capacitance, C_j, which, in turn, increases the junction photovoltage and thus the photoexcited electron-hole pairs [Melnikov et al. (2010)]. Under modulated excitation this increase in photocarrier-wave density improves the image contrast: As shown in Fig. 12, the carrierographic camera image of the mc-Si solar-cell fragment exhibits much better contrast which allows the resolution of fine features associated with the presence of grain boundaries.

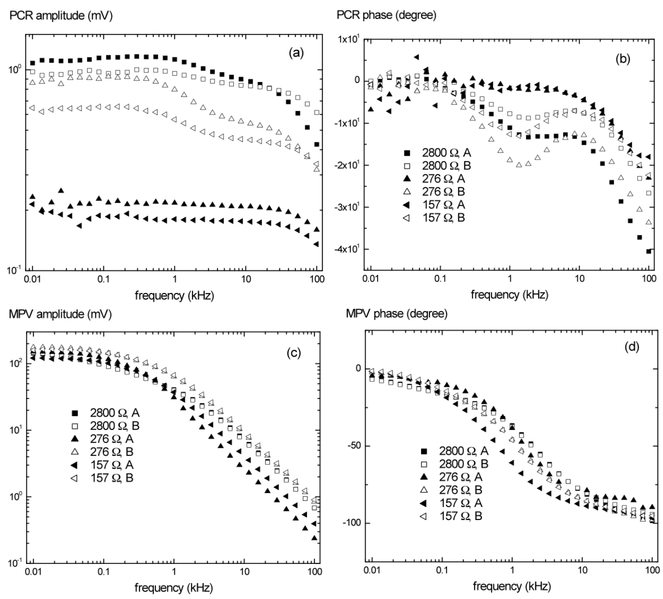

Figure 11. *PCR and MPV frequency scans of the solar cell imaged in Figure 10 at points outside (point A) and inside the damaged area (point B). Laser beam peak power: 30.9 mW, beam spotsize: ~ 400 µm.*

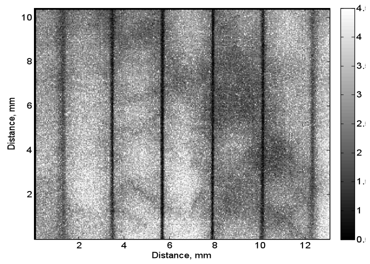

Figure 12. *Lock-in carrierographic camera amplitude image of a solar cell fragment.*

4. Conclusions

A combined imaging methodology involving modulated photovoltage (MPV) and photocarrier radiometry (PCR) of industrial multi-crystalline Si solar cells has been demonstrated. Point-by-point coordinate-scanned and lock-in InGaAs camera-based PCR carrierographic imaging has been introduced as a quantitative non-contacting and non-destructive methodology, with contrast derived from diffuse photo-carrier-wave transport and recombination processes in solar cells. Aided by its strong correlation to the frequency-scanned MPV ($V_{ph}(f)$) signals, the frequency response of the PCR ($S_{PCR}(f)$) signal was found to depend on two characteristic time constants, the minority carrier recombination lifetime in the quasi-neutral region (bulk) and the RC time constant, τ_{RC} , controlled by junction capacitance, dynamic junction resistance and load resistance. It was also shown that lock-in carrierographic imaging if very sensitive to the grain boundary, defect and surface recombination-inducing structure of mc-Si solar cells. The new technique can yield quantitative information on the aforementioned time constants and has excellent potential application for on-line or off-line optoelectronic quality control and efficiency enhancement of solar cell fabrication parameters.

Acknowledgements

The authors are grateful to Enfoton Solar, Kokkinotrimithia, Cyprus, for supplying the solar cells for this research. The support of the Natural Sciences and Engineering Research Council of Canada (NSERC), the Canada Research Chairs (CRC) program, and the Cyprus Institute is gratefully acknowledged.

5. References

Breitenstein O., Bauer J., Trupke T., Bardos R.. "On the detection of shunts in silicon solar cell by photo- and electroluminescence imaging", *Progr. Photovoltaic: Res. Appl.* **16**, 2008, pp. 325-330.

Carstensen J., Schüt A., Föll H., ”CELLO FFT impedance analysis as a routine tool for identifying various defect types on crystalline silicon solar cells”, *Proceedings 24rd European Photovoltaic Solar Energy Conference,* 1AO.4.5, Hamburg 2009.

Fuyaki T., Kondo H., Yamasaki T., Takahashi Y., Uraoka Y.. Photographic surveying of minority carrier diffusion length in polycrystalline silicon solar cells by electroluminescence. *Appl. Phys. Lett.* **86**, 2005, p. 262108-1-3

Glatthaar M., Giesecke J., Kasemann M., Haunschild J., The M., Warta W., Rein S.. Spatially resolved determination of the dark saturation current of silicon solar cells from electroluminescence images. *J. Appl. Phys.* **105**, 2009, p. 113110-1-5.

Isenberg J., Riepe S., Glunz S., Warta W.. Imaging method for laterally resolved measurement of minority carrier densities and lifetimes: Measurement principle and first applications. *J. Appl. Phys*. **93**, 2003, p. 4268-4275

Kampweth H., Trupke T., Weber J. W., Augarten Y. Advanced luminescence based effective series resistance imaging of silicon solar cells. *Appl. Phys. Lett.* **93**, 2008, p. 202102-1-3.

Kasemann M., Kwapil W., Giesecke J., Michl B., The M., Wagner J.-M., Bauer J., Schütt A., Carstensen J., Kampwerth H., Gundel P., Schubert M.C., Bardos R. A., Föll H., Nagel H., Würfel P., Trupke T., Breitenstein O., Warta W., Glunz S.W. Progress in silicon solar cell characterization with infrared imaging methods. *Proceedings 23rd European Photovoltaic Solar Energy Conference (23rd EU PVSEC),* WIP, Munich, Germany, 2008, p. 965-973.

Macdonald D., Tan J., Trupke T. Imaging interstitial iron concentration in boron-doped crystalline silicon using photoluminescence. *J. Appl. Phys.* **103**, 2008, p. 073710-1-7.

Mandelis A. Coupled ac photocurrent and photothermal reflectance response theory of semiconducting p-n junctions. I. *J. Appl. Phys.* **66**, 1989, p. 5572-5583.

Mandelis A. “*Diffusion-Wave Fields: Mathematical Methods and Green Functions”,* Chap. 9, Springer, New York, 2001.

Mandelis A., Batista J. and Shaughnessy D. Infrared photocarrier radiometry of semiconductors: Physical principles, quantitative depth profilometry, and scanning imaging of deep subsurface electronic defects. *Phys. Rev. B* **67,** 2003, p. 205208-1-18.

Melnikov A., Mandelis A., Tolev J., and Lioudakis E. Infrared photocarrier radiometry, modulated photovoltage and electrical characteristics of polycrystalline Si solar cells. *IOP J. Phys. Conf. Ser.* **214**, 2010, p. 012111-1-5

Munakata C. and Honma N. Non-destructive method for measuring cut-off frequency of a p-n junction with a chopped photon beam. *Jap. J. Appl. Phys.* **20**, 1981, p. L856-L585.

Shubert M. C., Riepe S., Bermejo S., Warta W. Determination of spatially resolved trapping parameters in silicon with injection dependent carrier density imaging. *J. Appl. Phys.* **99**, 2006, p. 114908-1-6.

Trupke T., Bardos R. A., Shubert M. C., Warta W. Photoluminescence imaging of silicon wafers. *Appl. Phys. Lett*. **89**, 2006, p. 044107-1-3.

Würfel P., Trupke T., Puzzer T., Schäffer E., Warta W., Glunz S. W.. Diffusion length of silicon solar cells from luminescence images. *J. Appl. Phys.* **101,** 2007, p. 123110-1-10.

Zhang S-Y. and Cheng J-C., “Theoretical studies of AC photothermal and AC electrothermal responses of semiconductor p-n junction devices”, *Semicond. Sci. Technol.* **6**, 1991, pp. 670-678.